

1 **Semi-solid Compression of Nano/Micro-Particle Reinforced Al-Cu**
2 **Composites: An *In Situ* Synchrotron Tomographic Study**

3
4 **Wei Wang ^a, Enyu Guo ^{a, b, *}, A. B. Phillion ^c, Dmitry G. Eskin ^d,**
5 **Tongmin Wang ^{a, b}, Peter D Lee ^e**
6

^a Key Laboratory of Solidification Control and Digital Preparation Technology
(Liaoning Province), School of Materials Science and Engineering,
Dalian University of Technology, Dalian 116024, China

^b Ningbo Institute of Dalian University of Technology, No.26 Yucai Road,
Jiangbei District, Ningbo, China, 315016

^c Department of Materials Science and Engineering, McMaster University, Hamilton,
L8S 4L7, Canada

^d Brunel Centre for Advanced Solidification Technology, Brunel University London,
Uxbridge, Middlesex UB8 3PH, UK

^e Department of Mechanical Engineering, University College London,
London WC1E 7JE, UK

7
8
9
10
11
12 **Submitted to**

13 **Materialia**

14 **In revised version**

15 **June 30, 2020**
16
17
18

19 Correspondence information:

20 * Enyu Guo (Dr./Prof.): eyguo@dlut.edu.cn; Tel.: +86(0)411-84709500
21
22

Abstract

Four-dimensional fast synchrotron X-ray tomography has been used to investigate the semi-solid deformation of nano- and micro-particle reinforced aluminum-copper composites (Al-10 wt% Cu alloy with ~1.0 wt% Al₂O₃ nano and ~1.0 wt% Al₂O₃ micro particles). Quantitative image analysis of the semi-solid deformation behavior of three alloys (base, nano- and micro-particle reinforced) revealed the influence of the particulate size on both microstructural formation and dominant deformation mechanisms. The results showed that initial void closure and incubation period were present in the particle-free and nano-particle reinforced Al-Cu composite during semi-solid compression, while the micro-particle reinforced alloy only showed continual voids growth and coalescence into cracks. The results suggest that the nano-particle reinforced composite have the best hot-tearing resistance amongst the three alloys. Improved hot-tear performance with nano-particulate reinforcement was attributed to the small liquid channel thickness, fine grain size which alters the distribution/morphology of the liquid channels, more viscous inter-dendritic liquid, and fewer initial voids.

Keywords: Metal matrix composites; Semi-solid deformation; Dilatancy; Hot-tearing

1. Introduction

Metal matrix composites (termed as MMCs) have attracted increasing attention in aerospace and automotive industries because of their outstanding properties including higher strength and wear resistance as compared to conventional particle-free lightweight alloys [1-4]. Casting (e.g. stir casting [5], squeeze casting [6, 7] and die casting [8]) is one of the widely used preparation methods to manufacture MMCs. Semi-solid processing [9] has also been used in order to obtain a uniform distribution of the added particles. It is well known that the particles significantly influence microstructure, processing defects, and properties including grain size [10, 11], hot tearing [12-18], viscosity [19, 20] and porosity [21, 22]. Therefore, studies of MMCs during semi-solid deformation are vital to improve our understanding of the semi-solid structural evolution mechanisms.

The addition of reinforcing particles to an alloy usually modifies its semi-solid constitutive behavior due to the presence of reinforcements at grain boundaries and their effect on grain refinement [11, 23]. Zhang et al. [11] showed that while the addition of TiB₂ particles reduced the hot-tearing susceptibility of Al-5 wt% Cu alloy via grain refinement, the reinforcing particles also increased the liquid viscosity thus lowering the feeding rate [11, 20], increasing hot-tearing susceptibility.

It is vital to have insight into the semi-solid microstructural response to the imposed deformation in the materials service and their fabrication due to the strains and stress induced by shrinkage and thermal contraction during the conventional casting and semi-solid processing [24-26]. Tzimas et al. [27] studied the semi-solid compression deformation mechanism of AA2014 and Al-10 wt% Cu alloys with equiaxed microstructure at the solid fraction above 60%, and evaluated the effect of strain rate, solid fraction and grain size on semi-solid deformation behavior at different deformation stages. However, the authors paid little attention to the microstructural changes under deformation and thus a detailed semi-solid deformation mechanism was not revealed. Due to the complex, heterogeneous interaction and deformation of the three phases (solid grains, interdendritic liquid phase, and voids), a few *in situ* observations of microstructural changes have been carried out to study semi-solid deformation mechanisms. Farup et al. [28] observed and recorded the hot-tearing of an organic succinonitrile-acetone alloy by using a microscope, but there are differences between metallic alloys and organic alloys such as the formation of the final eutectic and oxides, and thus the conclusion obtained by the succinonitrile-acetone alloy needs

further verification. Recently, Davidson et al. [29] observed the dynamic deformation behavior of Al-Cu alloys during solidification and tensile load by optical microscope, and they found that hot-tearing started at a low load with high solid fraction (90%). However, only two dimensional changes to the microstructure can be obtained via optical microscope, and organic model alloys do not possess the same mechanical and material physical properties as the metallic alloys. With wider availability of X-ray detection technology, improved methods have been developed to directly investigate the microstructural evolution of alloys during semi-solid deformation. Su et al. [16] combined *in situ* X-ray radiography of semi-solid Al-Cu alloy deformation at 40~70% solid fraction with simulations to capture the key microstructural feature evolution. In their study, a novel and coupled lattice Boltzmann method, discrete element method (LBM-DEM) mode, was established to simulate and verify the complex liquid behavior and local stresses. However, the studies using X-ray radiography were performed under low spatial resolution (2.5 $\mu\text{m}/\text{pixel}$), and the real 3D morphology in materials was not revealed.

With the further development of synchrotron radiation techniques, the improved temporal and spatial resolution greatly promoted the use of *in situ* studies to study metals in the semi-solid state. *In situ* X-ray tomography of tensile deformation of semi-solid Al-8 wt% Cu alloys was reported by Terzi et al. in 2009 [30], but the grain size was very large. Phillion et al. [31] studied the semi-solid tensile deformation of Al-12 wt% Cu alloys through synchrotron X-ray radiography images, and summarized the deformation process of three different stages under tension. Puncreobutr et al. [13] directly observed the damage accumulation of semi-solid Al-15 wt% Cu alloys through fast synchrotron X-ray micro-tomography during isothermal tensile deformation, and they found that voids grew and coalesced from the top region to the center of the sample, and that the final growth of voids was caused by insufficient liquid feeding. Very recently, Cai et al. conducted uniaxial compression [14] and indentation [15] of semi-solid Al-15 wt% Cu via fast synchrotron X-ray tomography. They combined a digital volume correlation technique with synchrotron experiments to analyze the microstructural response to various strains and finally to reveal semi-solid deformation mechanism. They found that different stages of semi-solid compression were present and the multitude of deformation mechanisms occurred at a microstructural level, such as liquid flow, voids/cracking, dilatancy, and intra-granular deformation. Karagadde et al. [24] observed *in situ* transgranular liquation cracking in localized indentation of Al-

15 wt% Cu globular microstructures using a similar synchrotron method. All the mentioned studies have helped us better understand the deformation mechanisms during semi-solid deformation of alloys. However, our understanding of the semi-solid deformation mechanisms in particle reinforced metal matrix composites is still limited as no *in situ* studies have been documented.

In this study, we investigate the semi-solid microstructural evolution and deformation behavior of an Al-10 wt% Cu alloy with and without Al₂O₃ reinforcing particles. The deformation behavior was quantified via fast synchrotron X-ray tomography to investigate the influence of nano- and micro- particles. A bespoke thermomechanical rig used in previous studies was used to perform the experiments [13, 14]. The mechanical behavior was correlated to the microstructure, the motion of the interdendritic liquid phase, and the formation and growth of voids. The differences in void evolution, liquid channel thickness and variation in transverse cross-sectional area between the three sample compositions are compared and discussed.

2. Experimental methods

2.1 Materials

Three alloys were prepared for semi-solid compression: (1) Al-10 wt% Cu alloy (termed as P-free alloy); (2) Al-10 wt% Cu alloy with ~1.0 wt% Al₂O₃ nano-particles (termed as NP composite; average particle size of ~50 nm) and (3) Al-10 wt% Cu alloy with ~1.0 wt% Al₂O₃ micro-particles (termed as MP composite; average particle size of ~13 μm). 99.97% pure aluminum and an Al-50wt% Cu master alloy were used as starting materials. After introduction of particles (wrapped in aluminum foil) and their mixing in the melt with a titanium impeller at 400 rpm, ultrasonic treatment was applied for ~15 min to both particle-containing alloys at ~100-150 °C above the liquidus temperature of the alloys to disperse the particles. The ultrasonic processing was performed using a niobium sonotrode under an ultrasonic wave with a peak-to-peak amplitude of 30 μm and a frequency of 17.5 kHz (a water-cooled magnetostrictive transducer at 3 kW power). The alloys were then cast into a preheated steel mold. Finally, test cylindrical samples of ~1.8 mm diameter and ~3.5 mm height were machined from the cast ingots.

2.2 Testing apparatus and procedures

Semi-solid compression tests were performed using a bespoke mechanical test rig

[13] known as the P2R, which was designed for *in situ* X-ray tomographic mechanical experiments [14, 20]. A laser-based heating system was used to heat the sample [32]. Each sample was heated to a semi-solid temperature of ~ 570 °C, corresponding to a liquid volume fraction of $\sim 25\%$ (Note: the liquid volume fraction was measured and determined by analysis of the 3D images), at a rate of 40 °C/min and then held isothermally for 10 min. Then, the compression displacement rate was set at ~ 0.5 $\mu\text{m/s}$. Each tomography scan contained 1001 projections with an exposure time of 30 ms and took ~ 37 s to complete the data collection. The time interval between tomography scans was ~ 50 s before the start of the next tomography scan.

The tomography experiments were carried out at the TOMCAT beamline of Swiss Light Source (SLS, Swiss) [33] utilizing a monochromatic X-ray beam with a photon energy of 38.6 keV. A PCO Edge 5.5 camera with the resolution of 1.7 $\mu\text{m/pixel}$, together with a LuAg: Ce single-crystal scintillator was used to record the projected images.

2.3 3D image reconstruction and quantification

For reconstructing the 3D tomographic datasets, a filtered back-projection algorithm was used [34]. Avizo (FEI VSG, France) and ImageJ (US NIH, Bethesda, MD USA) [35] software packages were used for image processing. The 3D non-local mean filter [36] and 3D median filter algorithms were used to maintain edges while reducing noise, which was followed by registration using a 3D affine registration approach. Global thresholding was used to segment the images into solid, liquid and void by Otsu [37] and Moments [38] methods after application of a background detection correction algorithm to improve segmentation of the features. Voids smaller than 10 voxels could be noise and were removed from the dataset. The local thickness of the liquid channels was determined using the Skeletons module in Avizo [39]. Quantification of the cross-sectional area and void percentage changes were acquired by using BoneJ [40], an ImageJ plugin. The height (l_i , where i is the tomography sequence) of the sample was measured from the 3D tomographic volumes, and was used to calculate the true bulk axial strain ($\epsilon = \ln \frac{l_i}{l_0}$) [14]. Note that l_0 is the height of the sample before compression. Grain size was measured in 2D longitudinal cross sections using the line intersection method.

3. Results

Qualitative Observations

Figure 1 shows centre-line longitudinal slices of the P-free alloy, NP composite and MP composite during the compression experiments. For each material, images of 3-4 load steps are shown. In this figure, the α -Al dendrites are in gray, the Cu-enriched interdendritic liquid is in white, and the voids are in black. These datasets were selected as they reveal critical changes occurring within the semi-solid microstructure. Initially there are only a few voids visible in the P-free alloy and NP composite (Figure 1(a), (d)). At low strain ($\epsilon = 0.030$; Figure 1(b) and (e)), there does not appear to have been an increase in the number nor volume of internal voids. At a moderate strain ($\epsilon = 0.095$; Figure 1(c)), the voids are seen to be growing and increasing in number in the P-free alloy, whereas they do not appear to change significantly in the NP composite (Figure 1(f)). Even at a large strain, the pores in the NP composite ($\epsilon = 0.433$; Figure 1(g)), appear to be small and distributed. The MP composite has contrastingly different behaviour. Void nucleation and growth are already occurring at low strain (Figure 1(i)) to form large micropores, and they have grown and coalesced significantly by the moderate strain level (Figure 1(j)). At the final strain of $\epsilon = 0.178$, the cracks formed in the MP composite are concentrated (Figure 1(k)).

Significant dilation of this material is also observed during the deformation process, which mainly occurs where voids grow and nucleate. The mid-height transverse slices are shown in Supplementary Figure 1 for all three materials, to show the process of dilation. The interdendritic channels dilate, increasing in width with increasing strain as indicated by the orange arrows in Figure 1. This is most obvious for the MP composite. In addition, the interdendritic liquid channels in the samples are much thicker where voids grow greatly. This is also indicated by the orange arrows in Figure 1.

The evolution of voids at different stages can be more directly observed from 3D rendered images. Figure 2 shows these with increasing strain in the three samples at the same levels of strain as Figure 1; the voids are rendered in color by size with different scaling used for each sample. In the P-free alloy (Figure 2(a-c)), it can be seen that the size and number of voids at the strain of $\epsilon = 0.030$ has actually decreased as compared to the initial state (Figure 2(a)). At the strain of $\epsilon = 0.095$, a great number of voids is seen to have appeared near the compression platen, with increased size and dilation also occurring in the same region. A similar phenomenon occurs in the NP composite (Figure

3(d-g)): in the strain range from $\varepsilon = 0.030$ to $\varepsilon = 0.094$ there is an incubation period prior to void growth. Voids of MP composites (Figure 2(h-k)) are two or three orders of magnitude larger than in the other two samples. In Figure 2(k), voids have coalesced due to their rapid growth and the largest size is measured to be $8 \times 10^8 \mu\text{m}^3$.

Quantitative Observations

Figure 3 compares the change in total cross section area including voids and void percentage of the different alloys with increasing compression. By examining Figure 3(a), (c), and (e), it can be seen that dilation of all three samples becomes more and more obvious with increasing strain. Combining these graphs with their counterparts (Figure 3(b), (d), and (f)), it is seen that the positions of dilation are consistent with the main locations of void growth. Comparing the black and red lines in Figures 3(b) and (d), a period of initial void closure, i.e. the void percentages at $\varepsilon = 0$ are clearly larger than those at $\varepsilon = 0.03$ for the P-free alloy and NP composite. This matches the qualitative observations of Figure 2. In contrast, the void percentage within the cross section increases constantly with the strain for the MP composite.

Figure 4 compares the evolution of total void percentage of the three materials with true axial strain, as determined by 3D datasets, in order to examine the evolution in voids/pores. The Y-axis is given in the logarithmic scale to show the three curves on the same graph. Beginning with the undeformed state, it is seen that the MP composite contained a much larger percentage of pre-existing voids (blue line, 1.01%) as compared to both the P-free alloy (red line, 0.13%) and the NP composite (black line, 0.03%). These pre-existing pores will start to change upon loading. For the MP composite, the void fraction is seen to grow continually with increasing compressive deformation to 16.11% as the true axial strain changes from $\varepsilon = 0$ to $\varepsilon = 0.178$. For the P-free alloy and NP composite, void growth behaves differently and is significantly less than the MP composite. The void percentages of both materials are seen to first decrease, then fluctuate within a small value range and finally increase rapidly. The rapid growth of voids begins at a strain of $\varepsilon = 0.075$ for the P-free alloy, while it begins at a strain of $\varepsilon = 0.295$ for the NP composite.

Typical morphology and sizes of pores in the early stages of deformation for each alloy are also given in Figure 4. As seen, voids Pf_2 and NP_2 are smaller than voids Pf_1 and NP_1 , respectively, suggesting the initial closure of voids upon loading, whereas void MP_2 is much bigger than void MP_1 , demonstrating void growth with compression

in the MP composite. As the ‘2’ voids were all acquired at different true axial strains, this comparison in void size and shape should be viewed as qualitative only.

Figure 5 shows the quantified thickness frequency distribution of local interdendritic liquid channels at various strain conditions for the three materials. The analysis region consists of a volume, $510 \times 510 \times 510 \mu\text{m}^3$, near the center of dilation. As can be seen, the frequency distribution of the liquid channels thicknesses is similar in all three materials in the initial state (Figure 5(a)). With increasing deformation first to the low strain (Figure 5(b) and then the moderate strain (Figure 5(c)), the large liquid channels ($>8 \mu\text{m}$) are seen to be growing in size and in frequency in the MP composite while the percentage of smaller channels ($< 8 \mu\text{m}$) is reduced. In contrast, little change in the liquid channel distribution is observed in the corresponding curves for the P-free alloy and NP composite. Comparing the curves at the final strain (Figure 5(d)), shows that the percentage of thick liquid channels ($>8 \mu\text{m}$) in the MP composite greatly exceeds those for the NP composite. It is noted that the distribution of liquid channels exhibits a Gaussian-like morphology for all the samples at all levels of strain, with the maximum number of liquid channels having a thickness value of 4-6 μm .

4. Discussion

Semi-solid Deformation Mechanisms:

Previous X-ray imaging studies of semi-solid deformation, both compression [14] and tension [13, 31], have identified three distinct deformation stages for Al alloys. For compression, the three stages are: I. Initial void closure; II. Incubation; III. Final rapid growth [14]. This three-stage deformation mode has also been observed in the present experiments, specifically within the P-free alloy and NP composite. Figure 6(a-d) schematically shows the microstructural evolution for the three stages for the P-free alloy and NP composite that was observed qualitatively in Figures 1 and 2 and quantified in Figures 4 and 5.

- Stage 1: In the initial stages of deformation, the interdendritic channels gradually broaden, Figure 5, likely because of the increasing compression pressure within the liquid and feeding of the liquid into gaps; the grains are also known to undergo minor plastic deformation [15, 41]. However, as was shown in Figure 4, the voids may also shrink due to translation of the external loads through the liquid channels to the void surfaces, as well as dilation.

- Stage II: In the incubation stage, the void percentage fluctuates within a certain range value, as was seen in Figure 4. As deformation further proceeds, liquid cannot distribute the continuously accumulated stress. Grains start to translate and rotate (this can be found in Supplementary Figure 2), leading to the formation of gaps. A similar phenomenon was also reported by Cai et al. [14, 15]. As liquid feeding is occurring [20], there is a dynamic balance between void growth and liquid feeding, resulting in the fluctuation of void volume.
- Stage III: When the true axial strain/shear stress reaches a critical point, the voids start to grow rapidly through fast self-growth coalescence activities, Figure 4. Similar deformation stages were previously observed in the semisolid compression of Al-15 wt% Cu [14] whose initial void percentage ($\sim 0.11\%$ for Al-15 wt% Cu) is comparable to the P-free alloy (0.13%) in this study.

Figure 6(e-h) shows schematically the observed compressive deformation for the MP composite. The main difference between the P-free alloy / NP composite and the MP composite is that the MP composite does not show an initial void closure and incubation period, as voids persistently grow and the void percentage is increasing.

The observed semi-solid compression behaviour can also be compared to similar behaviour in tension. For tension, the three stages can be summarized as [42]: I. Strain localization; II. Semi-solid necking in combination with void nucleation and growth; III. Coalescence and final fracture. Compressive and tensile behaviour are similar in that interdendritic liquid flow towards the location of voids/cracks with increasing loading; therefore, voids will grow and coalesce together. However, there is no initial void-closure stage in tension as the voids continually nucleate and increase in volume.

Some of the local deformation mechanisms can be summarized. In semi-solids, liquid feeds persistently when grains are pulled apart, and voids also keep growing because the solid-liquid interfacial energy is of a magnitude order smaller than the gas-liquid interfacial energy [30]. Liquid is more likely to be sucked into the Cu-enriched interdendritic liquid. During semi-solid deformation, dilation is an important phenomenon, as seen in the present study, which is attributed to Reynolds dilatancy effects due to localization of shear bands [43, 44]. Dilation of the sample manifestly occur where liquid flows into interdendritic gaps [45]. The flow of Cu-rich interdendritic liquid also causes remelting, as the local Cu concentration increases, reducing the liquidus temperature, melting the primary phase (see Supplementary

Figure 2) [14, 46].

Influence of particles on hot tearing susceptibility:

The results presented above indicate that the NP composite would possess the best hot-tearing resistance among the three sample conditions while the MP composite shows the worst hot-tearing resistance. Factors affecting hot-tearing of particle-reinforced composites include grain size [10, 11, 47] and particle size/content [11, 48]. In this study, the grain size of three materials was measured by an intersects method, and the results are summarized in Table 1.

Semi-solid alloys under compression have been shown to act as granular materials, both compressing the interdendritic spaces, and expanding them through dilation [17, 24, 44]. The fluid motion of the interdendritic liquid from one region to another is, therefore, a key mechanism for accommodating strain during compression. The efficacy of interdendritic feeding is dependent on: 1. the width of the interdendritic channels; 2. the viscosity of the interdendritic liquid, and 3. the distance over which feeding has to occur. The addition of particles to the melt can change all of these. Firstly, the particles can act as grain refiners, changing both the channel width and length. Secondly, the particles alter the viscosity.

Looking first at grain size, the NP composite grains are ~19% smaller than MP composite and P-free alloy. This would result in a difference in the morphology and thickness of the Cu-enriched interdendritic liquid channels (as illustrated in Figure 5), which in turn further affects the fluidity and feeding to voids/damage during compression. With finer grain size, the interdendritic liquid is more uniformly distributed before deformation and at the initial deformation stage, less torturous shape of the channels can better feed interdendritic gaps via the suck-in effect upon loading [11]. Smaller grains are also easier to rotate and accommodate the imposed strain, therefore offering better intrinsic resistance to hot cracking.

In addition, the reinforcing particles are known to increase the viscosity of liquid in semi-solid metals. Due to low wettability between particles and metals, most particles would be found at the grain boundaries and eutectic regions after complete solidification [23]. In the MP composites, the particle size (~13 μm) is mostly larger than the liquid channel thickness. Therefore, particles will exist within the interdendritic liquid or at the solid-liquid interface. Zhang et al. studied the hot-tearing susceptibility of $\text{TiB}_2/\text{Al-5 wt\% Cu}$, and found that the fracture surface was partly covered by large TiB_2 particles (~1 μm) agglomerates, which lowered the fluidity of liquid metal and

hindered the intergranular feeding mechanically [11]. In addition, due to lower wettability between ceramic particles and the interdendritic liquid phase, the existence of a three phase interface increases the surface tension and interfacial energy [30], leading to an increase in viscosity (reducing fluidity), thus also resulting in an increased hot-tearing susceptibility. The decline of the liquid phase feeding ability accelerates the growth of initial voids and the formation of new voids. With strain increasing, the liquid phase cannot feed the growing voids, and the void percentage shows a growing trend without periodic growth. As for the NP composite, the nano-particle size is ~ 50 nm, far smaller than that of the liquid channel thickness. Ultrasonic cavitation treatment of the melt greatly reduces particle agglomeration, minimizing the impact of particles on the fluidity of the interdendritic liquid phase. As a result, the effect of the nanoparticles on the feeding ability is minimized.

The different initial void distribution and size in the three sample conditions may also bring about effects on the deformation and hot-tearing behavior. In this study, the initial void percentages of the P-free alloy and NP composite are 0.13% and 0.04%, respectively, and the general size of those pre-existing pores is relatively small, while the initial void percentage of the MP composite is 1.01%, which is far higher than the other two samples. In addition, the size of the pre-existing pores in the MP composite is much larger than in the P-free alloy and NP composite (see Figure 2 and 4). Therefore, the relatively large size and volume of voids, coupled with the restricted feeding, may increase the probability of nucleation and growth of hot cracks in the MP composite upon external loading as cracks are easier to merge and grow. However, the detailed examination of hot tearing development is outside the scope of the current study and would need further investigation.

Sistaninia et al [49] and Su et al [50] have performed some related simulation work to study the semi-solid compression behavior of alloys. For example, Sistaninia et al. [49] developed a 3D coupled hydromechanical granular model that can be used to directly predict the hot tear formation and stress-strain behavior in metallic alloys during solidification. Simulation results show that the pressure drop, and consequently hot tear formation, depends also on the compressibility of the mushy zone skeleton, in addition to the lack of liquid feeding and semi-solid deformation. Su et al. [50] coupled the lattice Boltzmann method and discrete element method to study the semi-solid compression behavior of semi-solid Al-Cu alloys and compared the results with the experimental observations. With the simulation work, factors that affect the shear rate dependence of the volumetric strain and transitions are explored. Similar work, as

mentioned above, can be possibly performed by incorporating the particles in the liquid channel into the physical model in the future study, and then the influence of particles on the deformation behavior of semi-solid particle-reinforced metal matrix composites can be further explored. New insights into the semi-solid deformation mechanisms can then be gained.

5. Conclusions

In situ semi-solid compression of an Al-10wt% Cu alloy with and without Al₂O₃ nanoparticles or Al₂O₃ micro-particles was performed to compare the deformation tendencies using fast synchrotron X-ray tomography. The main findings are as follows:

1. Void evolutions of the NP composite and P-free alloy show three distinct stages: I. Initial void closure; II. Incubation period; III. Final rapid growth. On the contrary, voids in the MP composite keep growing during the whole deformation process. Dilation of all three samples was manifestly observed.
2. The void volume of the MP composite is one to two orders of magnitude larger than those of the NP composite and P-free alloy during the whole deformation process under similar strains.
3. The NP composite shows potentially best hot-tearing resistance among the three sample compositions because of the modified uniform dendritic network and better ability of liquid feeding due to refined dendritic grains and smoother interdendritic channels, as well as less affected liquid viscosity in the interdendritic region due to well-dispersed nanoparticles.

Acknowledgments

E. G and T. W acknowledge the financial support by the National Key Research and Development Program of China (No. 2017YFA0403803), National Natural Science Foundation of China (Nos. 51901034, 51525401, 51927801, 51974058) and LiaoNing Revitalization Talents Program (No. XLYC1808005). D. E acknowledges financial support from the ExoMet Project funded by the European Commission in the 7th Framework Programme (Contract FP7-NMP3-LA-2012– 280421) and EPSRC-funded project UltraMelt2 (EP/R011001/1). The experiments were funded by the EPSRC (EP/I02249X/1) and the Royal Academy of Engineering (CiET1819/10), and were performed at TOMCAT beamline of the Swiss Light Source (Paul Scherrer Institut, Switzerland, 20120463). We acknowledge both the beamline staff and Prof. Lee's group for performing the beamline experiments.

Declaration of interest

The authors declare no known competing interests.

Reference

- [1] G. Fan, L. Geng, H. Wu, K. Miao, X. Cui, H. Kang, T. Wang, H. Xie, T. Xiao, Improving the Tensile Ductility of Metal Matrix Composites by Laminated Structure: A Coupled X-Ray Tomography and Digital Image Correlation Study, *Scripta Mater.* 135 (2017) 63-67. <http://doi.org/10.1016/j.scriptamat.2017.03.030>
- [2] E. Guo, S. Shuai, D. Kazantsev, S. Karagadde, A.B. Phillion, T. Jing, W. Li, P.D. Lee, The Influence of Nanoparticles on Dendritic Grain Growth in Mg Alloys, *Acta Mater.* 152 (2018) 127-137. <http://doi.org/10.1016/j.actamat.2018.04.023>
- [3] M. Gao, Z. Chen, H. Kang, E. Guo, R. Li, Y. Fu, H. Xie, T. Wang, Microstructural Characteristics and Mechanical Behavior of B4cp/6061al Composites Synthesized at Different Hot-Pressing Temperatures, *J. Mater. Sci. Technol.* 35(8) (2019) 1523-1531. <http://doi.org/10.1016/j.jmst.2019.03.040>
- [4] M. Gao, H. Kang, Z. Chen, E. Guo, P. Peng, T. Wang, Effect of Reinforcement Content and Aging Treatment on Microstructure and Mechanical Behavior of B4cp/6061al Composites, *Mater. Sci. Eng. A* 744 (2019) 682-690. <http://doi.org/10.1016/j.msea.2018.12.042>
- [5] J. Hashim, L. Looney, M.S.J. Hashmi, Metal Matrix Composites: Production by the Stir Casting Method, *J. Mater. Process. Tech.* 93 (1999) 1-7. [http://doi.org/10.1016/S0924-0136\(99\)00118-1](http://doi.org/10.1016/S0924-0136(99)00118-1)
- [6] M.R. Ghomashchi, A. Vikhrov, Squeeze Casting: An Overview, *J. Mater. Process. Tech.* 101(1-3) (2000) 1-9. [http://doi.org/10.1016/s0924-0136\(99\)00291-5](http://doi.org/10.1016/s0924-0136(99)00291-5)
- [7] J.W. Kaczmar, K. Pietrzak, W. Wlosinski, The Production and Application of Metal Matrix Composite Materials, *J. Mater. Process. Tech.* 106(1-3) (2000) 58-67. [http://doi.org/10.1016/s0924-0136\(00\)00639-7](http://doi.org/10.1016/s0924-0136(00)00639-7)
- [8] P.K. Rohatgi, A. Daoud, B.F. Schultz, T. Puri, Microstructure and Mechanical Behavior of Die Casting Az91d-Fly Ash Cenosphere Composites, *Compos. Part A* 40(6-7) (2009) 883-896. <http://doi.org/10.1016/j.compositesa.2009.04.014>
- [9] M.C. Flemings, Behavior of Metal Alloys in the Semisolid State, *Metall. Trans. B* 22(3) (1991) 269-293. <http://doi.org/10.1007/bf02651227>
- [10] S. Lin, C. Aliravci, N.I.O. Pekgulyuz, Hot-Tear Susceptibility of Aluminum Wrought Alloys and the Effect of Grain Refining, *Metall. Mater. Trans. A* 38A(5) (2007) 1056-1068. <http://doi.org/10.1007/s11661-007-9132-7>
- [11] X.B. Zhang, J. Sun, M.L. Wang, Y.J. Zhang, N.H. Ma, H.W. Wang, Hot Tearing Susceptibility of Tib₂-Reinforced Al-5cu Matrix Composite, *J. Compos. Mater.* 50(15) (2016) 2059-2071. <http://doi.org/10.1177/0021998315601487>
- [12] D. Fuloria, P.D. Lee, An X-Ray Microtomographic and Finite Element Modeling Approach for the Prediction of Semi-Solid Deformation Behaviour in Al-Cu Alloys, *Acta Mater.* 57(18) (2009) 5554-5562. <http://doi.org/10.1016/j.actamat.2009.07.051>
- [13] C. Puncreobutr, P.D. Lee, R.W. Hamilton, B. Cai, T. Connolley, Synchrotron Tomographic Characterization of Damage Evolution During Aluminum Alloy Solidification, *Metall. Mater. Trans. A* 44(12) (2012) 5389-5395. <http://doi.org/10.1007/s11661-012-1563-0>
- [14] B. Cai, S. Karagadde, L. Yuan, T.J. Marrow, T. Connolley, P.D. Lee, In Situ Synchrotron Tomographic Quantification of Granular and Intragranular Deformation During Semi-Solid

453 Compression of an Equiaxed Dendritic Al–Cu Alloy, *Acta Mater.* 76 (2014) 371-380.
 454 <http://doi.org/10.1016/j.actamat.2014.05.035>

455 [15] B. Cai, P.D. Lee, S. Karagadde, T.J. Marrow, T. Connolley, Time-Resolved Synchrotron
 456 Tomographic Quantification of Deformation During Indentation of an Equiaxed Semi-Solid Granular
 457 Alloy, *Acta Mater.* 105 (2016) 338-346. <http://doi.org/10.1016/j.actamat.2015.11.028>

458 [16] T.C. Su, C. O'Sullivan, T. Nagira, H. Yasuda, C.M. Gourlay, Semi-Solid Deformation of Al-Cu
 459 Alloys: A Quantitative Comparison between Real-Time Imaging and Coupled Lbm-Dem Simulations,
 460 *Acta Mater.* 163 (2019) 208-225. <http://doi.org/10.1016/j.actamat.2018.10.006>

461 [17] K.M. Kareh, P.D. Lee, R.C. Atwood, T. Connolley, C.M. Gourlay, Revealing the Micromechanisms
 462 Behind Semi-Solid Metal Deformation with Time-Resolved X-Ray Tomography, *Nat. Commun.* 5 (2014)
 463 4464. <http://doi.org/10.1038/ncomms5464>

464 [18] S. Bhagavath, B. Cai, R. Atwood, M. Li, B. Ghaffari, P.D. Lee, S. Karagadde, Combined
 465 Deformation and Solidification-Driven Porosity Formation in Aluminum Alloys, *Metall. Mater. Trans. A*
 466 50A(10) (2019) 4891-4899. <http://doi.org/10.1007/s11661-019-05378-8>

467 [19] A. Mortensen, I. Jin, Solidification Processing of Metal Matrix Composites, *Int. Mater. Rev.* 37(3)
 468 (1992) 101-128. <http://doi.org/10.1179/imr.1992.37.1.101>

469 [20] C. Puncreobutr, P.D. Lee, R.W. Hamilton, A.B. Phillion, Quantitative 3d Characterization of
 470 Solidification Structure and Defect Evolution in Al Alloys, *Jom* 64(1) (2012) 89-95.
 471 <http://doi.org/10.1007/s11837-011-0217-9>

472 [21] R.C. Atwood, S. Sridhar, W. Zhang, P.D. Lee, Diffusion-Controlled Growth of Hydrogen Pores in
 473 Aluminium–Silicon Castings: In Situ Observation and Modelling, *Acta Mater.* 48(2) (2000) 405-417.
 474 [http://doi.org/https://doi.org/10.1016/S1359-6454\(99\)00363-8](http://doi.org/https://doi.org/10.1016/S1359-6454(99)00363-8)

475 [22] M.J. Roy, D.M. Maijer, Analysis and Modelling of a Rotary Forming Process for Cast Aluminium
 476 Alloy A356, *J. Mater. Process. Tech.* 226 (2015) 188-204.
 477 <http://doi.org/10.1016/j.jmatprotec.2015.06.036>

478 [23] X.H. Chen, H. Yan, Solid-Liquid Interface Dynamics During Solidification of Al 7075-Al₂O₃np
 479 Based Metal Matrix Composites, *Mater. Des.* 94 (2016) 148-158.
 480 <http://doi.org/10.1016/j.matdes.2016.01.042>

481 [24] S. Karagadde, P.D. Lee, B. Cai, J.L. Fife, M.A. Azeem, K.M. Kareh, C. Puncreobutr, D. Tsivoulas,
 482 T. Connolley, R.C. Atwood, Transgranular Liquefaction Cracking of Grains in the Semi-Solid State, *Nat.*
 483 *Commun.* 6 (2015) 8300. <http://doi.org/10.1038/ncomms9300>

484 [25] M. Ahmadein, M. Wu, G. Reinhart, H. Nguyen-Thi, A. Ludwig, Modelling Al-4wt.%Cu as-Cast
 485 Structure Using Equiaxed Morphological Parameters Deduced from in-Situ Synchrotron X-Ray
 486 Radiography, *IOP Conf. Ser.: Mater. Sci. Eng.* 117 (2016) 012010. <http://doi.org/10.1088/1757-899x/117/1/012010>

487
 488 [26] A.J. Clarke, D. Tournet, Y. Song, S.D. Imhoff, P.J. Gibbs, J.W. Gibbs, K. Fezzaa, A. Karma,
 489 Microstructure Selection in Thin-Sample Directional Solidification of an Al-Cu Alloy: In Situ X-Ray
 490 Imaging and Phase-Field Simulations, *Acta Mater.* 129 (2017) 203-216.
 491 <http://doi.org/10.1016/j.actamat.2017.02.047>

492 [27] E. Tzimas, A. Zavaliangos, Mechanical Behavior of Alloys with Equiaxed Microstructure in the
 493 Semisolid State at High Solid Content, *Acta Mater.* 47(2) (1999) 517-528. [http://doi.org/10.1016/s1359-6454\(98\)00356-5](http://doi.org/10.1016/s1359-6454(98)00356-5)

494
 495 [28] I. Farup, J.M. Drezet, M. Rappaz, In Situ Observation of Hot Tearing Formation in Succinonitrile-
 496 Acetone, *Acta Mater.* 49(7) (2001) 1261-1269. [http://doi.org/10.1016/s1359-6454\(01\)00013-1](http://doi.org/10.1016/s1359-6454(01)00013-1)

497 [29] C. Davidson, D. Viano, L. Lu, D. StJohn, Observation of Crack Initiation During Hot Tearing, *Int.*
498 *J. Cast Met. Res.* 19(1) (2013) 59-65. <http://doi.org/10.1179/136404606225023291>

499 [30] S. Terzi, L. Salvo, M. Suéry, N. Limodin, J. Adrien, E. Maire, Y. Pannier, M. Bornert, D. Bernard,
500 M. Felberbaum, In Situ X-Ray Tomography Observation of Inhomogeneous Deformation in Semi-Solid
501 Aluminium Alloys, *Scripta Mater.* 61(5) (2009) 449-452.
502 <http://doi.org/10.1016/j.scriptamat.2009.04.041>

503 [31] A.B. Phillion, R.W. Hamilton, D. Fuloria, A.C.L. Leung, P. Rockett, T. Connolley, P.D. Lee, In Situ
504 X-Ray Observation of Semi-Solid Deformation and Failure in Al-Cu Alloys, *Acta Mater.* 59(4) (2011)
505 1436-1444. <http://doi.org/10.1016/j.actamat.2010.11.005>

506 [32] J.L. Fife, M. Rappaz, M. Pistone, T. Celcer, G. Mikuljan, M. Stampanoni, Development of a Laser-
507 Based Heating System for in Situ Synchrotron-Based X-Ray Tomographic Microscopy, *J. Synchrotron*
508 *Rad.* 19 (2012) 352-358. <http://doi.org/10.1107/s0909049512003287>

509 [33] U. Bonse, M. Stampanoni, A. Groso, A. Isenegger, G. Mikuljan, Q. Chen, A. Bertrand, S. Henein,
510 R. Betemps, U. Frommherz, P. Böhler, D. Meister, M. Lange, R. Abela, Trends in Synchrotron-Based
511 Tomographic Imaging: The Sls Experience, *Proc. SPIE*, 2006. <http://doi.org/10.1117/12.679497>

512 [34] S. Titarenko, V. Titarenko, A. Kyrieleis, P.J. Withers, A Ring Artifact Suppression Algorithm Based
513 on a Priori Information, *Appl. Phys. Lett.* 95(7) (2009). <http://doi.org/10.1063/1.3211956>

514 [35] C.A. Schneider, W.S. Rasband, K.W. Eliceiri, Nih Image to Imagej: 25 Years of Image Analysis,
515 *Nat. Methods* 9(7) (2012) 671-675. <http://doi.org/10.1038/nmeth.2089>

516 [36] A. Buades, B. Coll, J.M. Morel, A Non-Local Algorithm for Image Denoising, in: C. Schmid, S.
517 Soatto, C. Tomasi (Eds.), *Proc. Ieee Comput. Soc. Cond. Cpmput. Vis. Pattern Recognit.*(2005), pp. 60-
518 65. <http://doi.org/10.1109/CVPR.2005.38>

519 [37] N. Otsu, Threshold Selection Method from Gray-Level Histograms, *IEEE Trans. Syst. Man Cybern.*
520 9(1) (1979) 62-66. <http://doi.org/10.1109/tsmc.1979.4310076>

521 [38] W.H. Tsai, Moment-Preserving Thresholding-a New Approach, *Comput. Vision Graph. Image*
522 *Process.* 29(3) (1985) 377-393. [http://doi.org/10.1016/0734-189x\(85\)90133-1](http://doi.org/10.1016/0734-189x(85)90133-1)

523 [39] C. Fouard, G. Malandain, S. Prohaska, M. Westerhoff, Blockwise Processing Applied to Brain
524 Microvascular Network Study, *IEEE Trans. Med. Imaging* 25(10) (2006) 1319-1328.
525 <http://doi.org/10.1109/tmi.2006.880670>

526 [40] M. Doube, M.M. Klosowski, I. Arganda-Carreras, F.P. Cordelieres, R.P. Dougherty, J.S. Jackson, B.
527 Schmid, J.R. Hutchinson, S.J. Shefelbine, Bonej: Free and Extensible Bone Image Analysis in Imagej,
528 *Bone* 47(6) (2010) 1076-9. <http://doi.org/10.1016/j.bone.2010.08.023>

529 [41] A.B. Phillion, S.L. Cockcroft, P.D. Lee, A Three-Phase Simulation of the Effect of Microstructural
530 Features on Semi-Solid Tensile Deformation, *Acta Mater.* 56(16) (2008) 4328-4338.
531 <http://doi.org/10.1016/j.actamat.2008.04.055>

532 [42] A.B. Phillion, P.D. Lee, E. Maire, S.L. Cockcroft, Quantitative Assessment of Deformation-Induced
533 Damage in a Semisolid Aluminum Alloy Via X-Ray Microtomography, *Metall. Mater. Trans. A* 39a(10)
534 (2008) 2459-2469. <http://doi.org/10.1007/s11661-008-9584-4>

535 [43] R.F. Katz, M. Spiegelman, B. Holtzman, The Dynamics of Melt and Shear Localization in Partially
536 Molten Aggregates, *Nature* 442(7103) (2006) 676-9. <http://doi.org/10.1038/nature05039>

537 [44] C.M. Gourlay, A.K. Dahle, Dilatant Shear Bands in Solidifying Metals, *Nature* 445(7123) (2007)
538 70-3. <http://doi.org/10.1038/nature05426>

539 [45] W.J. Mead, The Geologic Role of Dilatancy, *J. Geol.* 33(7) (1925) 685-698.
540 <http://doi.org/10.1086/623241>

- [46] S. Ananiev, P. Nikrityuk, K. Eckert, Dendrite Fragmentation by Catastrophic Elastic Remelting, *Acta Mater.* 57(3) (2009) 657-665. <http://doi.org/10.1016/j.actamat.2008.10.004>
- [47] S. Li, K. Sadayappan, D. Apelian, Role of Grain Refinement in the Hot Tearing of Cast Al-Cu Alloy, *Metall. Mater. Trans. B* 44(3) (2013) 614-623. <http://doi.org/10.1007/s11663-013-9801-4>
- [48] J.F. Zhang, H. Andrä, X.X. Zhang, Q.Z. Wang, B.L. Xiao, Z.Y. Ma, An Enhanced Finite Element Model Considering Multi Strengthening and Damage Mechanisms in Particle Reinforced Metal Matrix Composites, *Compos. Struct.* 226 (2019). <http://doi.org/10.1016/j.compstruct.2019.111281>
- [49] M. Sistaninia, A. B. Phillion, J. M. Drezet, M. Rappaz, A 3D coupled hydromechanical granular model for simulating the constitutive behavior of metallic alloys during solidification, *Acta Mater.* 60(19) (2012) 6793-6803. <http://doi.org/10.1016/j.actamat.2012.08.057>
- [50] T.C. Su, C. O. Sullivan, H. Yasuda, C.M. Gourlay, Rheological transitions in semi-solid alloys: in-situ imaging and LBM-DEM simulations, *Acta Mater.* 191 (2020) 24-42. <http://doi.org/10.1016/j.actamat.2020.03.011>

Table

Table 1. Comparison of grain size for three samples measured by intersects method

	P-free alloy	NP composite	MP composite
Grain size (μm)	98 ± 7	77 ± 8	95 ± 8

Figures

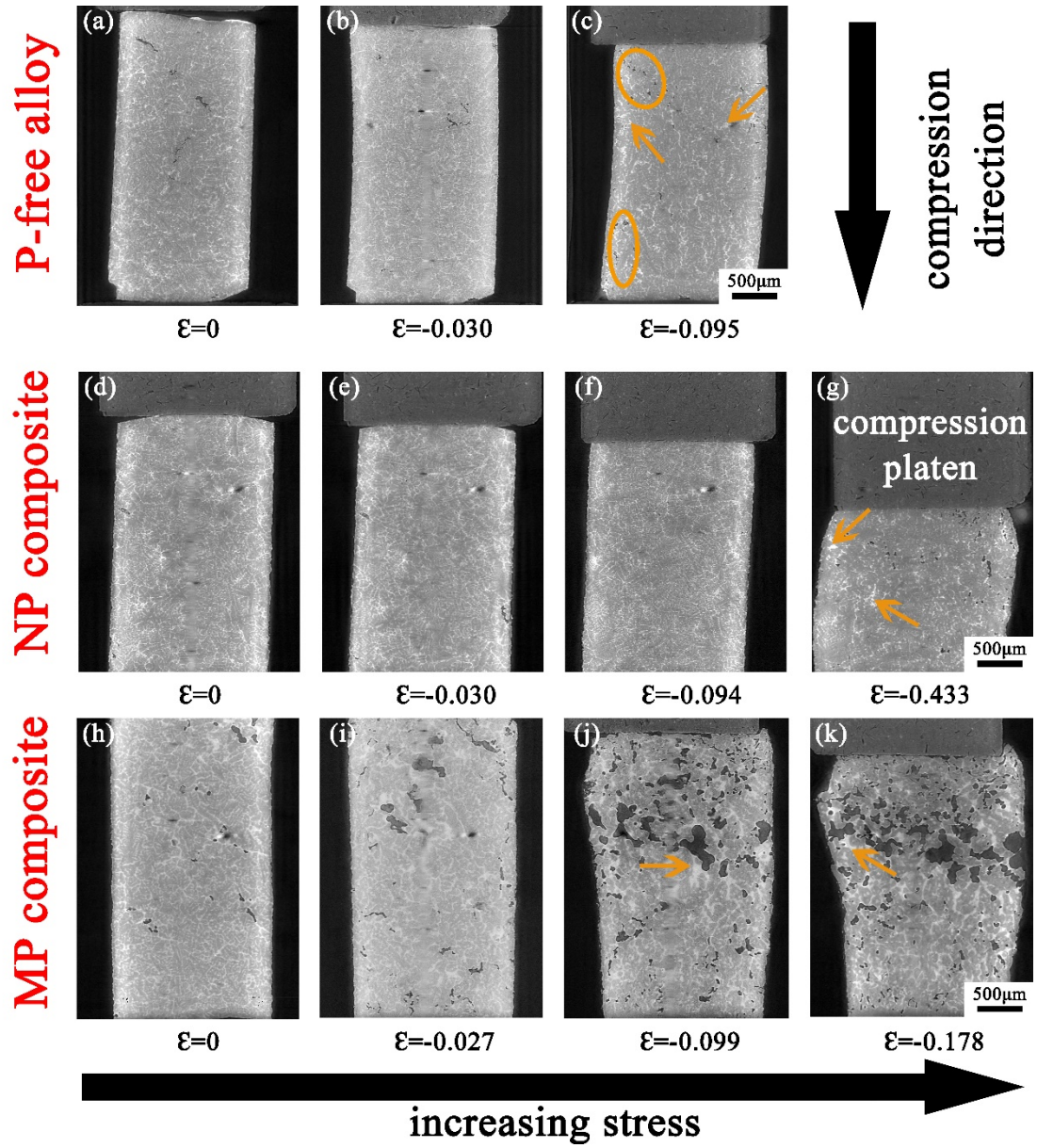
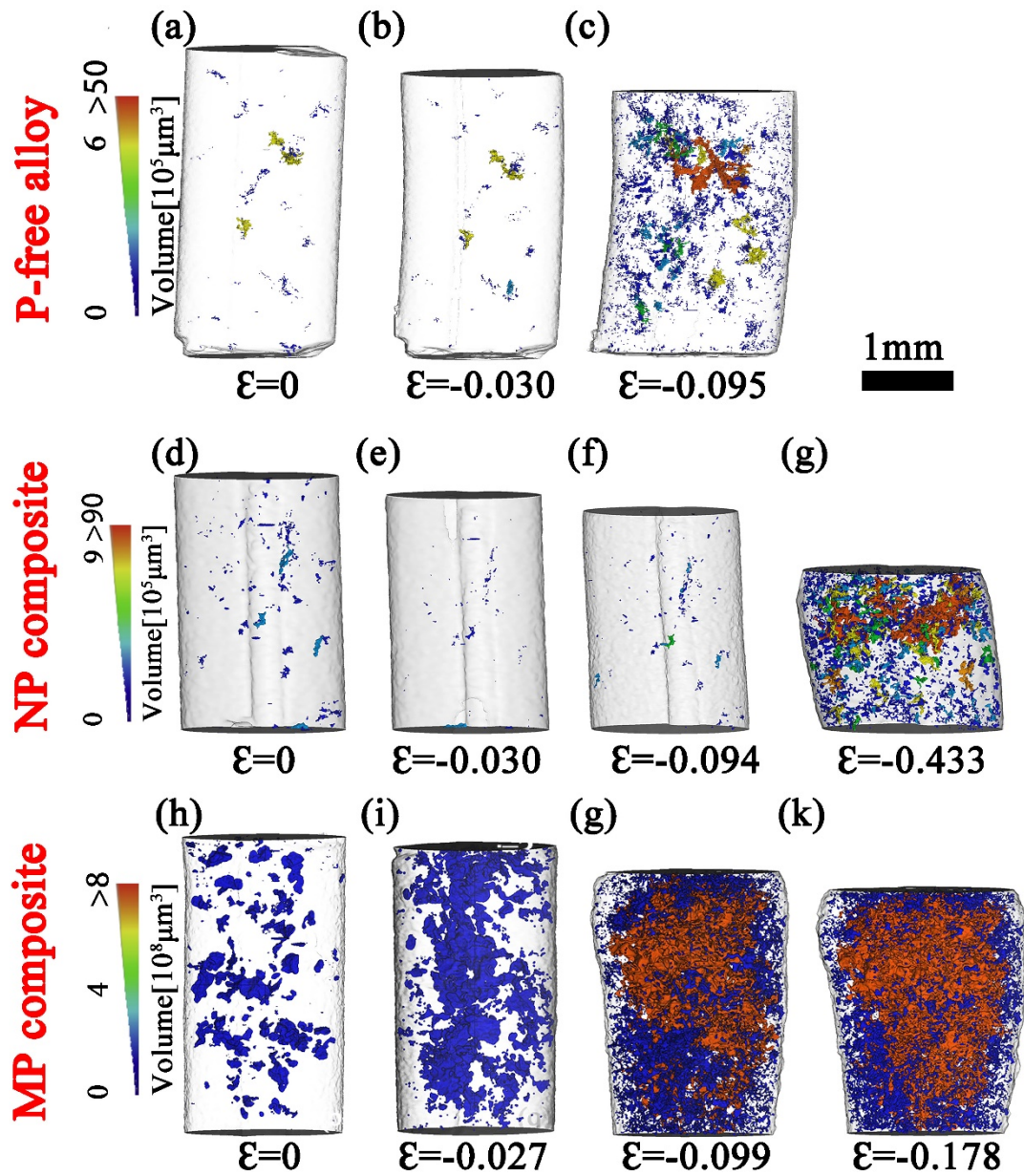


Figure 1. Longitudinal slices showing the deformation behavior of P-free alloy (a-c), NP composite (d-g) and MP composite (h-k) materials as a function of true axial strain during semi-solid compression. The elliptic circles and arrows represent areas-of-interest.



569

570

571

572

573

Figure 2. Evolution of voids colored according to their sizes during semi-solid compression of three samples with an increase in true axial strain. Images are for (a)-(c) P-free alloy, (d)-(g) NP composite, and (h)-(k) MP composite. Note the difference in scale of pore sizes.

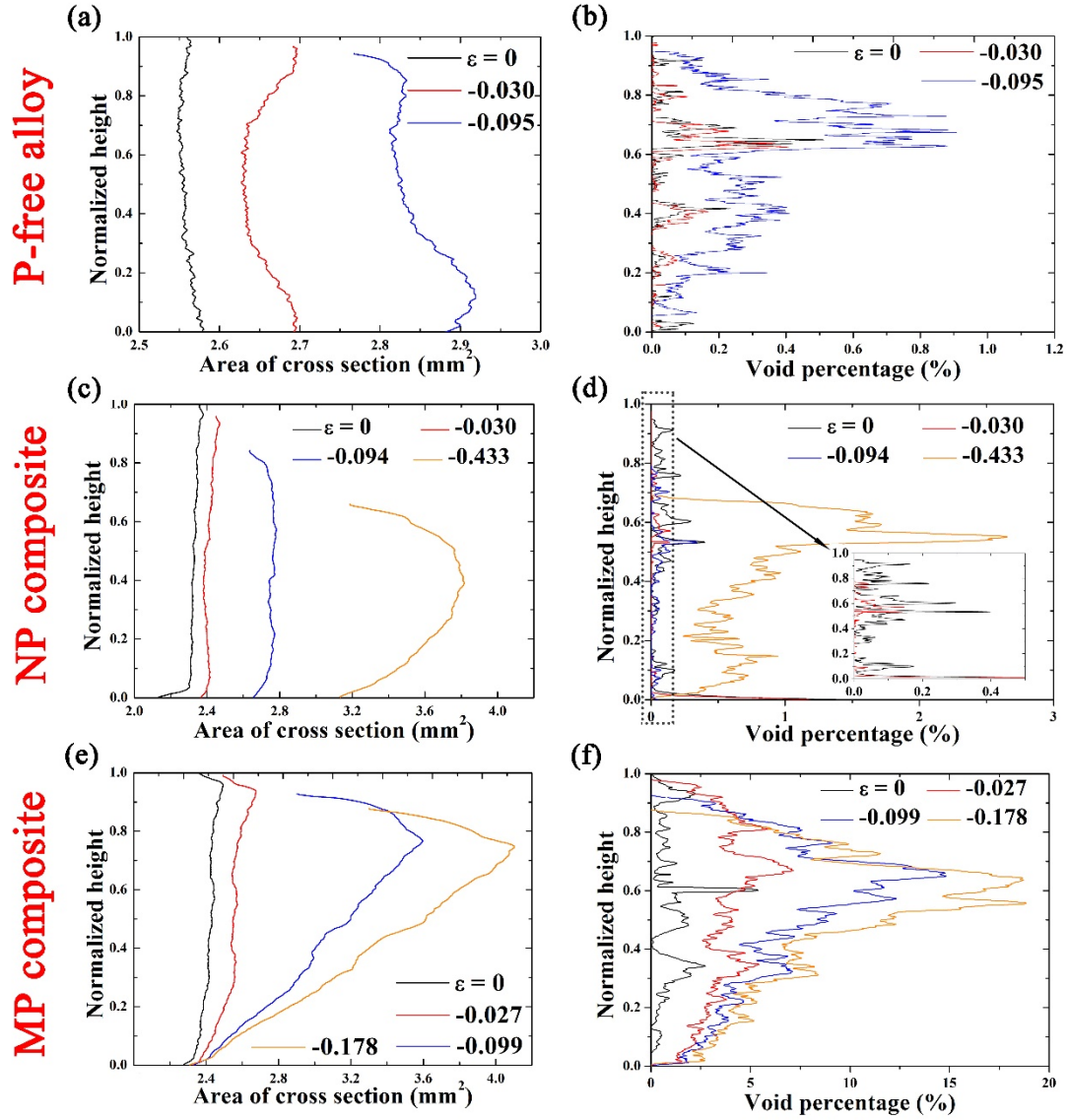


Figure 3. Variation in transverse cross-sectional area ((a), (c) and (e)) and void percentage ((b), (d) and (f)) along the normalized axis of compression with increasing strain. (a, b), (c, d) and (e, f) are for P-free alloy, NP composite, and MP composite, respectively. The inserts in (d) show the variations of void percentage in cross-sectional area at the initial deformation stages.

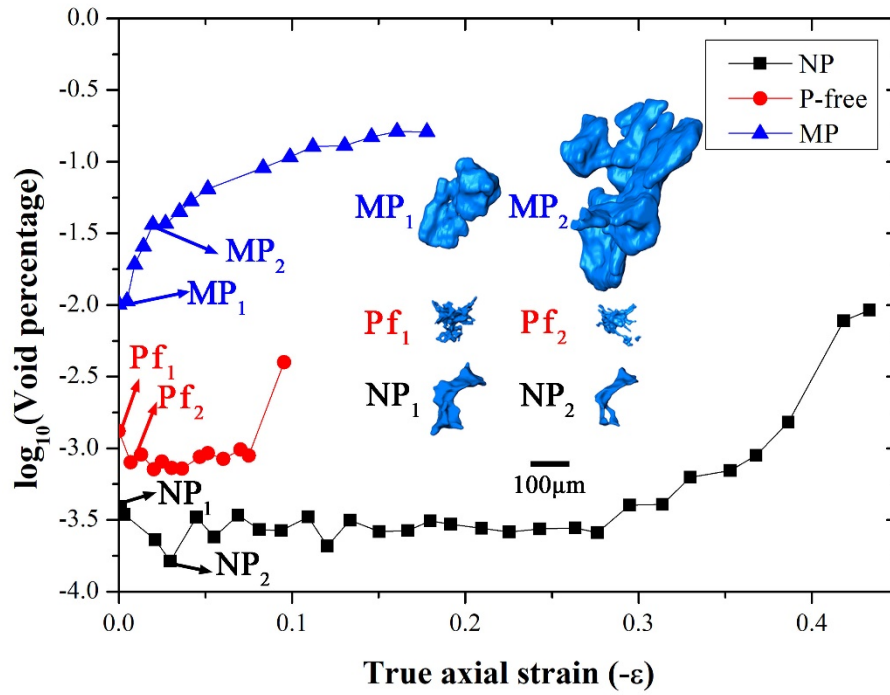


Figure 4. Evolution of void percentage for the P-free alloy, NP composite, and MP composite materials as a function of true axial strain. Inserted images Pf_{1/2}, NP_{1/2}, MP_{1/2} show examples of void changes at the early deformation stage of each sample. The negative sign on the x-axis denotes compressive deformation.

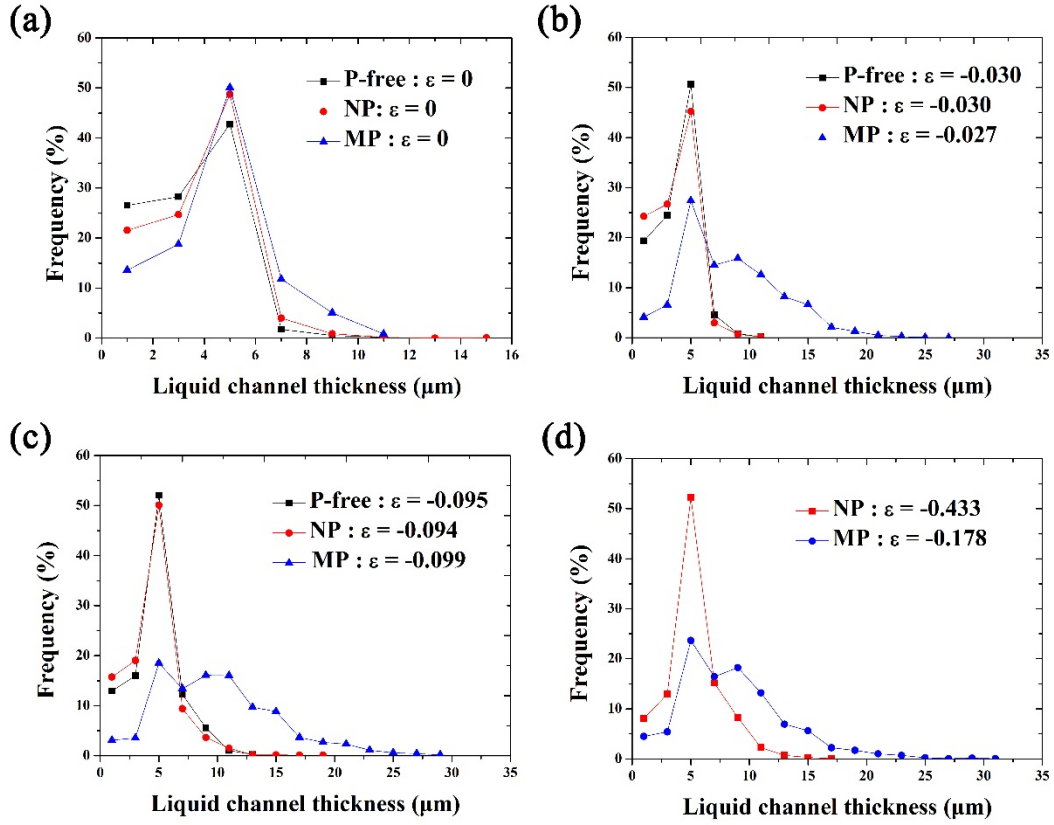


Figure 5. (a - d) Comparison in liquid channel thickness distribution within the central regions of the three sample conditions for (a) $\varepsilon = 0$, (b) $\varepsilon = \sim -0.030$, (c) $\varepsilon = \sim -0.100$, and (d) final strain, respectively

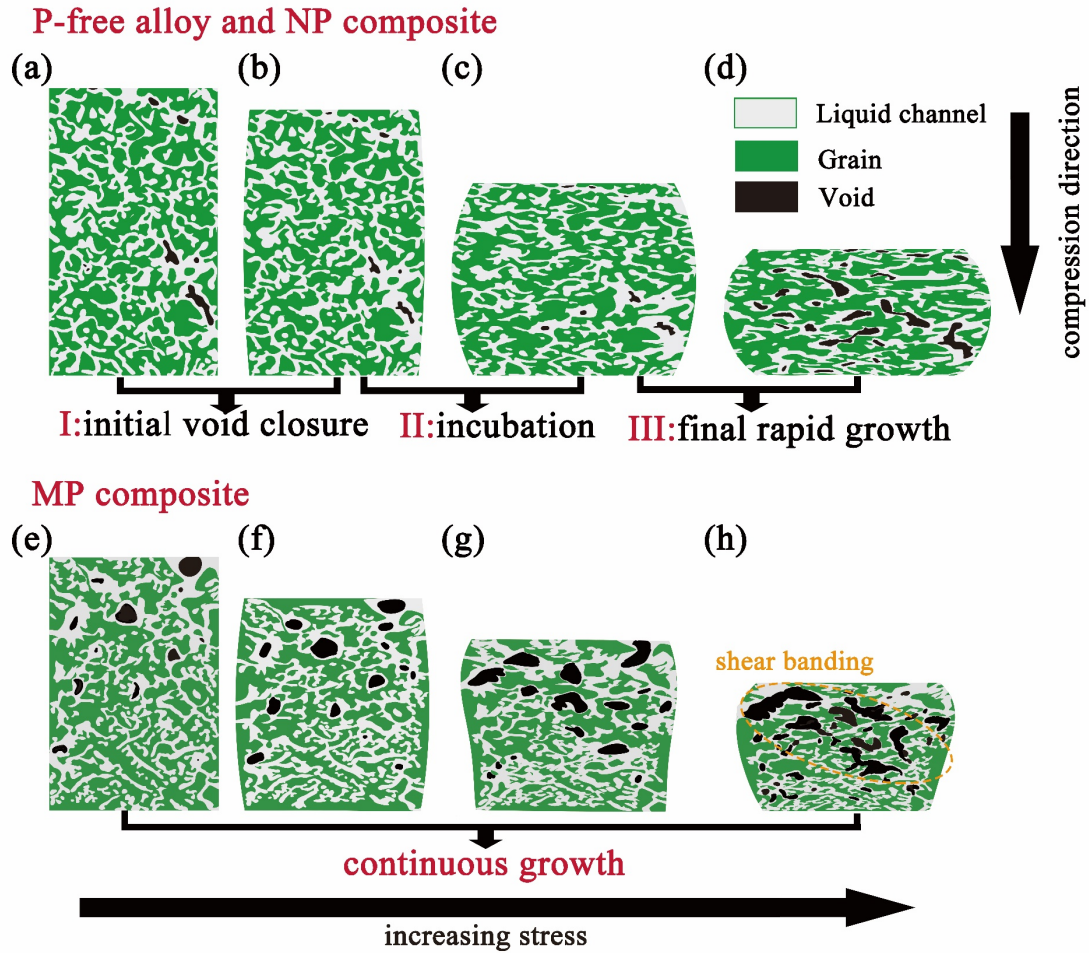
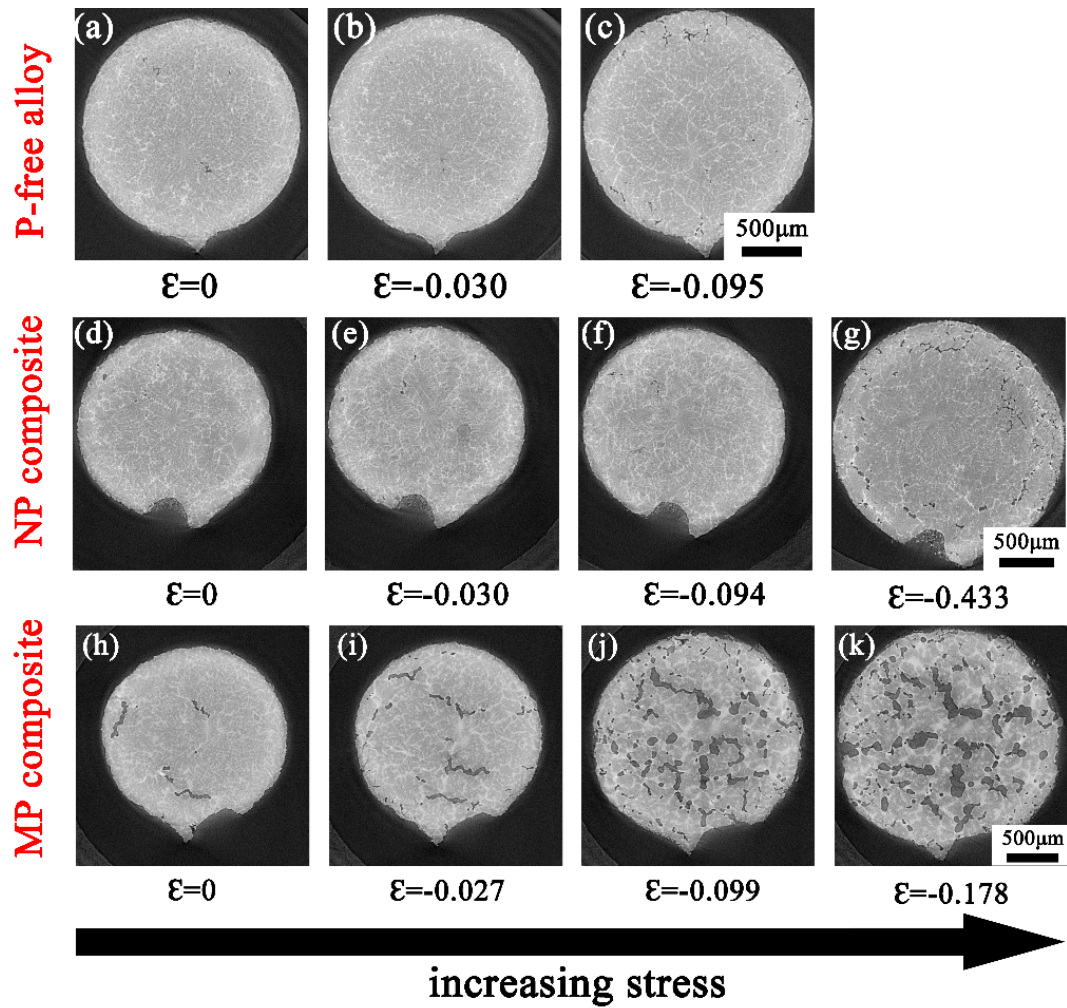
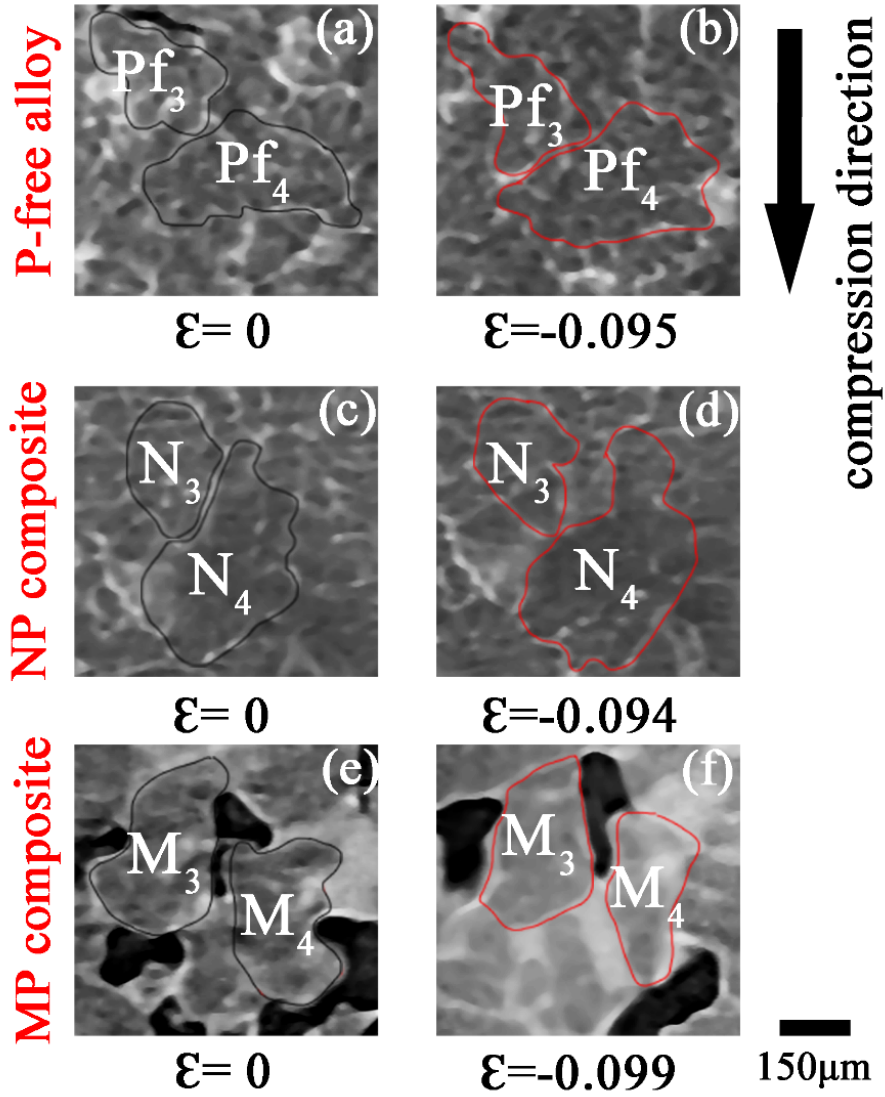


Figure 6. (a)-(d) Schematic diagram at granular and intragranular deformation of different stages during semi-solid compression; stage I (a-b): initial void closure at low strain; stage II (b-c): incubation at medium strain; stage III (c-d): final rapid growth at high strain. In the figure, the primary dendritic α -Al grains (α -Al), interdendritic liquid channel, and voids/pores are in green, white and black, respectively. (e)-(h) Schematic diagram at granular and intragranular deformation of MP composite during semi-solid compression: a continuing growth stage.

Supplementary Materials



Supplement-Figure 1. Mid-height transverse slices showing the deformation behaviors of (a-c) P-free alloy, (d-g) NP composite and (h-k) MP composite during semi-solid compression.



Supplement-Figure 2. Translation and rotation of local grains for three samples; Images are for (a) and (b) P-free; (c) and (d) NP composite; (e) and (f) MP composite. The grains marked by the black line are before deformation; the grains marked by the red line are during deformation.